Quantifying uncertainties in solar wind forecasting due to incomplete solar magnetic field information

The Astrophysical Journal, 986:166 (12pp), 2025 June 20 https://doi.org/10.3847/1538-4357/adcf9e

Quantifying Uncertainties in Solar Wind Forecasting due to Incomplete Solar Magnetic Field Information

Stephan G. Heinemann[1], Jens Pomoell[1], Ronald M. Caplan[2], Mathew J. Owens[3], Shaela Jones[4], Lisa Upton[5], Bibhuti Kumar Jha[5], and Charles N. Arge[4]
[1] Department of Physics, University of Helsinki, P.O. Box 64, 00014, Helsinki, Finland; stephan.heinemann@hmail.at
[2] Predictive Science Inc., 9990 Mesa Rim Road, Suite 170, San Diego, CA 92121, USA
[3] Space and Atmospheric Electricity Group, Department of Meteorology, University of Reading, Earley Gate, P.O. Box 243, Reading, RG6 6BB, UK
[4] Heliophysics Science Division, NASA Goddard Space Flight Center, Code 671, Greenbelt, MD 20771, USA
[5] Southwest Research Institute, Boulder, CO 80302, USA
Received 2025 March 21; revised 2025 April 14; accepted 2025 April 21; published 2025 June 16

Abstract

Solar wind forecasting plays a crucial role in space weather prediction, yet significant uncertainties persist duet to incomplete magnetic field observations of the Sun. Isolating the solar wind forecasting errors due to these effects is difficult. This study investigates the uncertainties in solar wind models arising from these limitations. We simulate magnetic field maps with known uncertainties, including far-side and polar field variations, as well as resolution and sensitivity limitations. These maps serve as input for three solar wind models: the Wang–Sheeley–Arge, the Heliospheric Upwind eXtrapolation, and the European Heliospheric FORecasting Information Asset. We analyze the discrepancies in solar wind forecasts, particularly the solar wind speed at Earth's location, by comparing the results of these models to a created ground truth magnetic field map, which is derived from a synthetic solar rotation evolution using the Advective Flux Transport model. The results reveal significant variations within each model with a root mean square error ranging from 59 to 121 km s^{-1}. Further comparison with the thermodynamic Magnetohydrodynamic Algorithm outside a Sphere model indicates that uncertainties in the different models can lead to even larger variations in solar wind forecasts compared to those within a single model. However, predicting a range of solar wind velocities based on a cloud of points around Earth can help mitigate uncertainties by up to 20%–77%.

Unified Astronomy Thesaurus concepts: Solar wind (1534); Solar magnetic fields (1503); Space weather (2037); Heliosphere (711)

1. Introduction

Space weather has become an integral part of modern life, influencing various aspects of daily activities. Any space weather forecast—whether for eruptive or recurrent events—relies on the assumption of a fundamentally accurate (zeroth-order) ambient solar wind. Consequently, solar wind forecasting, and especially solar wind modeling, must begin with this foundation as highlighted by A. W. Case et al. (2008).

To forecast space weather impacts at a high level, the ambient solar wind must be reliably understood, modeled, and predicted. Currently, a wide range of methods is employed for solar wind forecasting, including data-driven, empirical and semi-empirical approaches (e.g., T. Rotter et al. 2012, 2015; M. A. Reiss et al. 2016; M. Temmer et al. 2018; D. Milošić et al. 2023), hybrid and physics-based models (see M. J. Owens et al. 2008), and numerical modeling approaches ranging from one-dimensional to three-dimensional simulations (Z. Mikić et al. 1999; D. Odstrčil & V. J. Pizzo 1999; J. Pomoell et al. 2019; L. Barnard & M. Owens 2022). However, studies have highlighted significant uncertainties even in processes considered among the simplest in space weather forecasting, the ambient solar wind (e.g., L. K. Jian et al. 2015; J. Hinterreiter et al. 2019; M. A. Reiss et al. 2023).

Among all potential sources of uncertainty, the lack of concurrent observational coverage of the Earth–Sun system has been identified as a primary challenge (COSPAR ISWAT Roadmap; M. Temmer et al. 2023). This is because most models depend on a representation of the full-Sun surface radial magnetic field as input for forecasting the solar wind. However, the limited vantage points currently available routinely, primarily Earth, result in magnetic field maps that include inherent assumptions about the strength and distribution of the magnetic field, particularly in poorly observed regions such as the polar areas (P. Riley et al. 2019) and the solar far side (e.g., S. G. Heinemann et al. 2021; D. Yang et al. 2024).

To mitigate these limitations, two common approaches are widely used in the community. The first involves the creation of synoptic charts, which are constructed by effectively stacking bands of magnetic field observations near the central meridian over the course of a solar rotation. However, this method neglects the potential rapid evolution of the solar magnetic field, leading to an "aging effect" (S. G. Heinemann et al. 2021; A. Posner et al. 2021), where some parts of the map are significantly older than others. The second approach uses surface transport models to evolve the solar surface magnetic field observed from Earth, based on theoretical assumptions (e.g., C. N. Arge et al. 2010; L. Upton & D. H. Hathaway 2014a; D. Yang et al. 2024; R. M. Caplan et al. 2025). While these models account for magnetic flux transport processes, they still lack observational data from

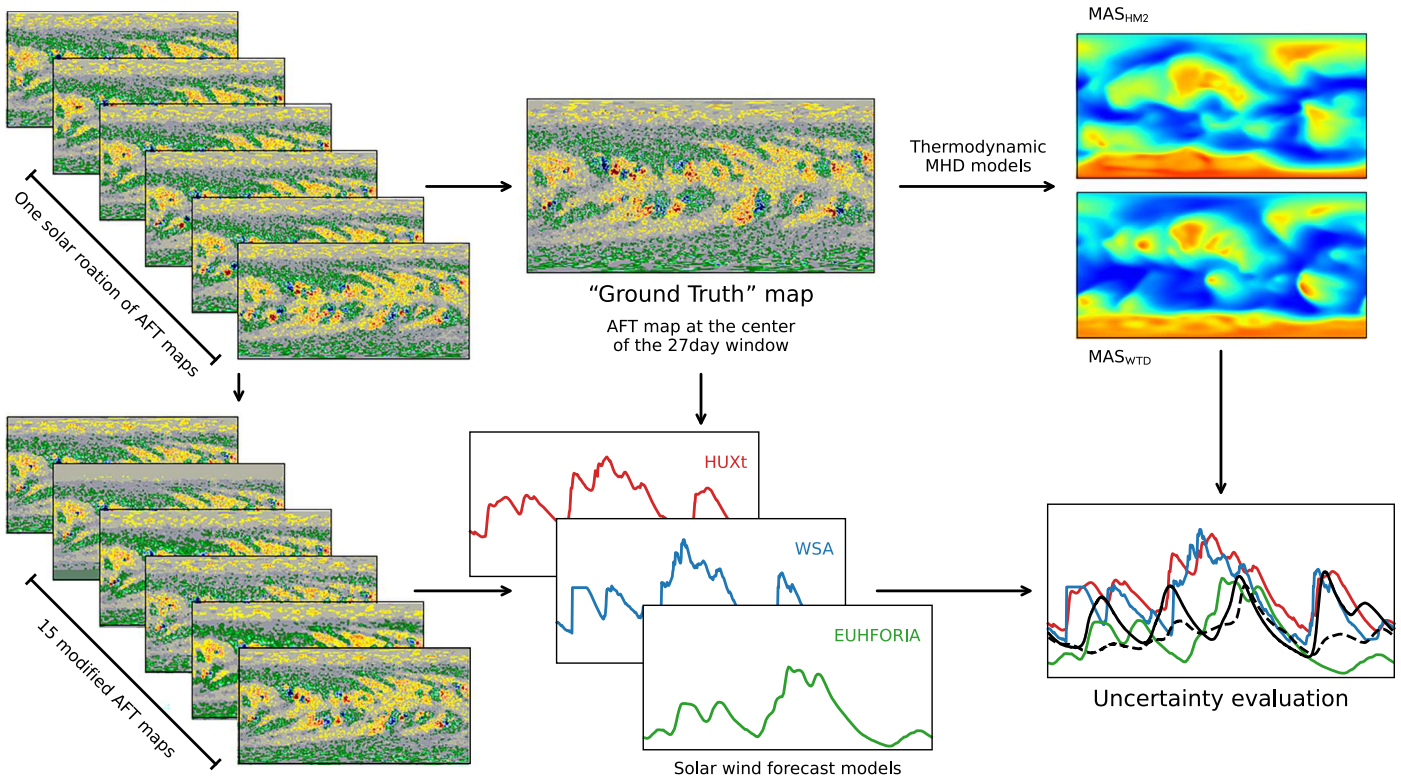

Figure 1. Schematic of the methodological approach used in this study. We begin by analyzing one solar rotation of artificial magnetic fields to determine the ground truth map and generate modified maps that account for observational uncertainties in 15 different ways. Next, we run three operational models with the modified maps `HUXt`, `WSA`, and `EUHFORIA`, and compare their results to those obtained from the ground truth map, as well as from the `MAS` simulations of the ground truth map.

unobserved regions of the Sun, where flux emergence and reconnection processes occur.

The most straightforward solution to these issues would be to directly observe the unmonitored regions of the Sun. Currently, the only instrument capable of partially observing the Sun's far side is the Photospheric and Magnetic Imager (PHI; S. K. Solanki et al. 2020) on board Solar Orbiter (SO; D. Müller et al. 2020). B. Perri et al. (2024) demonstrated that missing even a single far-side active region can significantly impact both local and global magnetic structures and C. Downs et al. (2025) used PHI data to improve eclipse simulations. However, due to the complexity of SO's orbit, comprehensive far-side coverage is rare, and not available in real time.

In this study, we investigate the uncertainties in solar wind forecasting arising from incomplete magnetic field information. To achieve this, we use a series of artificial magnetograms (similar to the one used in B. K. Jha & L. A. Upton 2024) designed to emulate the most prominent uncertainties present in magnetic charts commonly employed in space weather modeling. By inputting these magnetograms into three operational solar wind models, we quantify the uncertainties stemming from these specific sources over one artificial solar rotation. A general overview of the methodological approach of this study is shown in Figure 1.

2. Data

To quantify uncertainties from a specific origin, a ground truth must be established. In our case, this would ideally involve concurrent observations of the full solar magnetic field, which is currently not feasible. Therefore, we opted to use an artificial ground truth. Specifically, we simulate the magnetic field evolution over one solar rotation using the Advective Flux Transport (AFT) model (L. Upton & D. H. Hathaway 2014a). AFT has the ability to incorporate magnetic flux directly through data assimilation of magnetograms or by adding idealized bipoles to simulate active region emergence. In this case, we run AFT without data assimilation, and instead add synthetic active regions. Details of the model setup are provided in Appendix A.1. This approach yields 27 synthetic full-Sun magnetic field maps at a daily cadence with a resolution of 512×1024 pixels.

For this study, we assume that this set of maps represents the actual state of the Sun, i.e., the ground truth. From this set, we define the central map (day 13) as the ground truth map (Figure 2(a)). For this map, we can apply preprocessing routines to make it compatible as input for thermodynamic magnetohydrodynamic (MHD) modeling (for details, see Appendix A.2; Figure 2(b)).

Using this set of observations, we derive maps that simulate known uncertainties arising from incomplete observations of the full Sun. Broadly, these uncertainties can be categorized into three main types:

Far-side uncertainty. The standard method for creating solar maps for space weather modeling involves the use of synoptic charts. Synoptic charts are created by stacking overlapping 15° slices taken from the central meridian to produce a map of the entire Sun that includes active region at all longitudes (see, e.g., Figure 2(c)). Here, we have used all 27 AFT maps to create a synoptic chart that is constructed in the same manner as one created from daily observations. This approach mimics Earth as a single observation point.

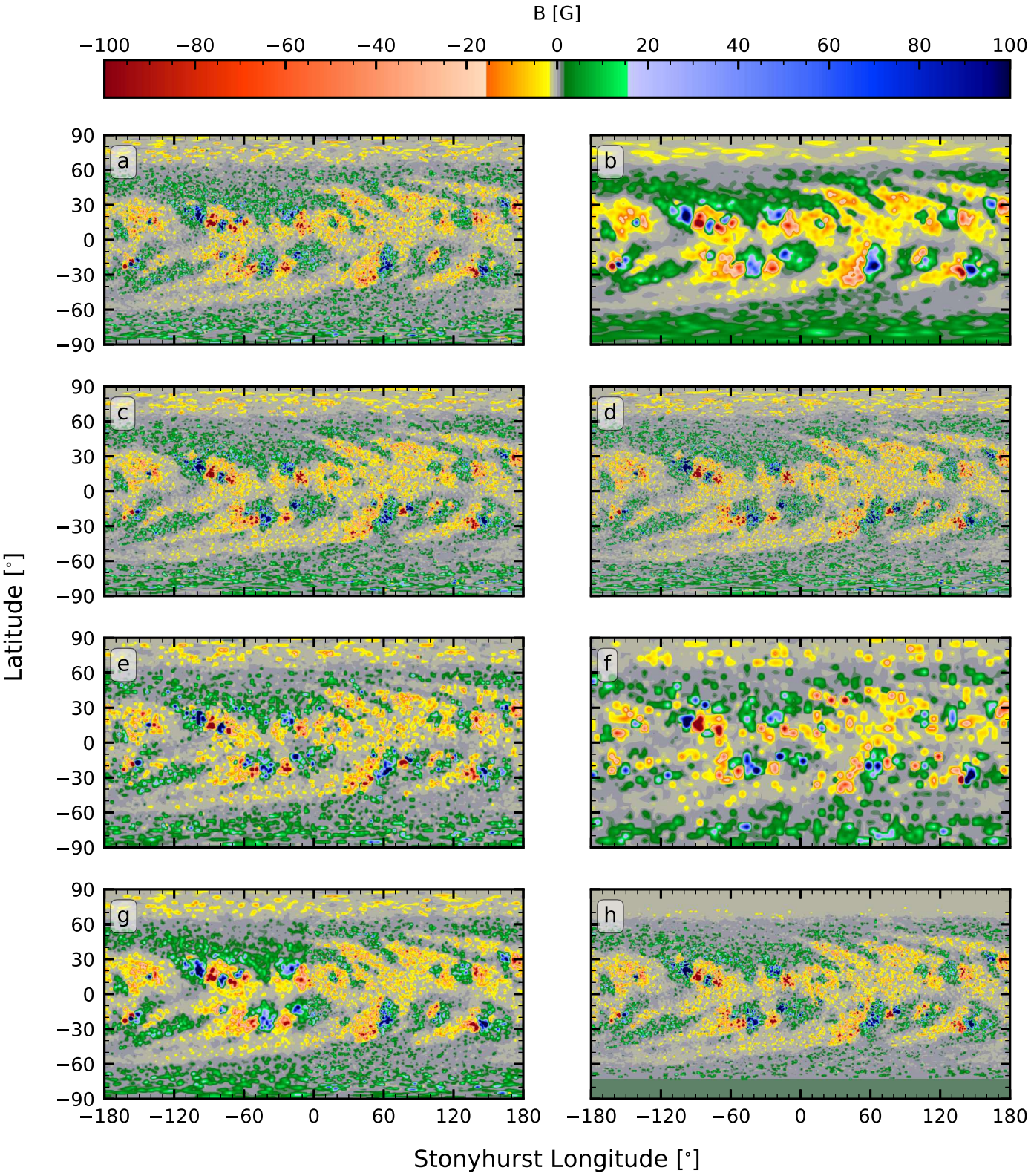

Figure 2. Magnetic maps used in this study. (a) The base or ground truth map. (b) The ground truth map modified for MAS model runs. (c) A synoptic chart created from a 27 day sample of maps. (d)–(f) Synoptic charts with varying resolutions: double, half, and quarter, respectively. (g) The ground truth map with increased smoothing as a function of distance from the Earth-facing point, simulating uncertainty in surface flux transport models. (h) A synoptic chart with uniform field strength applied in the polar regions.

In order to emulate the uncertainty due to the decreasing availability of magnetic data from Earth's vantage (as the flux rotates across the far side without being updated), we apply a Gaussian filter to the ground truth map to create a synthetic surface flux transport model-like map. The Gaussian filter has a kernel size that increases as a function of distance from the assumed Earth-facing location (i.e., the most recent map) in the direction of the solar rotation. We note that this smoothing

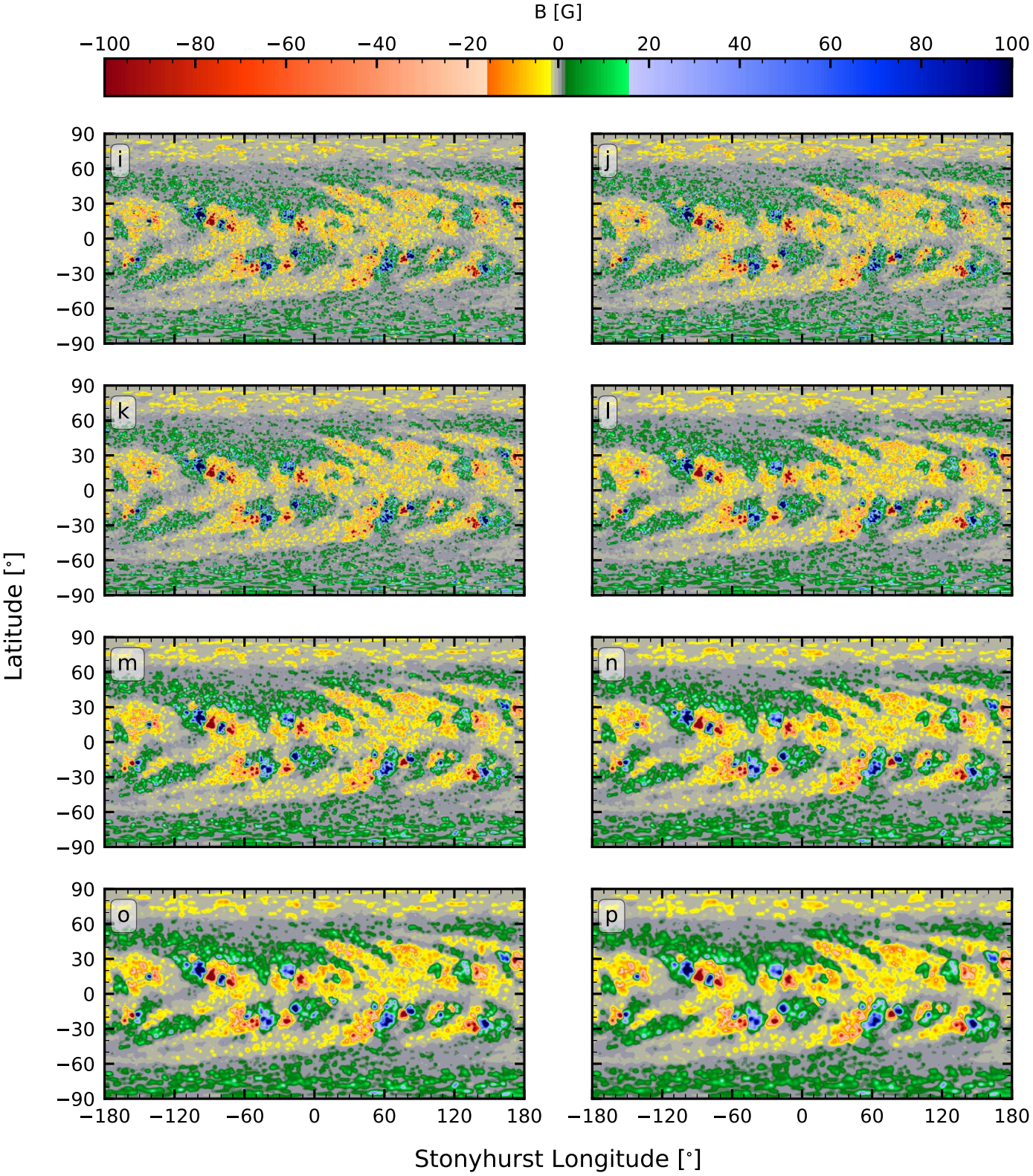

Figure 3. Continuation from Figure 2. (i) and (j) Synoptic charts with modified polar fields, increased and decreased by ±30%, respectively. (k)–(p) Synoptic charts smoothed using Gaussian kernels of varying sizes: $0.^{\circ}5$, $1.^{\circ}0$, $1.^{\circ}5$, $2.^{\circ}0$, $2.^{\circ}5$, and $3.^{\circ}0$, respectively.

is particularly evident on smaller spatial scales, over time (Figure 2(g)).

Uncertainty of the polar fields. It is well known that polar fields are integral to heliospheric models, and their uncertainties may play a key role in addressing the issue of the missing open solar magnetic flux (e.g., P. Riley et al. 2019). To simulate this behavior, we increase and decrease the polar magnetic flux of the synoptic chart by ±30% using a $\sin^6$ function (Figures 3(i) and (j)). Additionally, we replicate the methodology used for the `hmi.mrdailysynframe_polfil_720s` data product

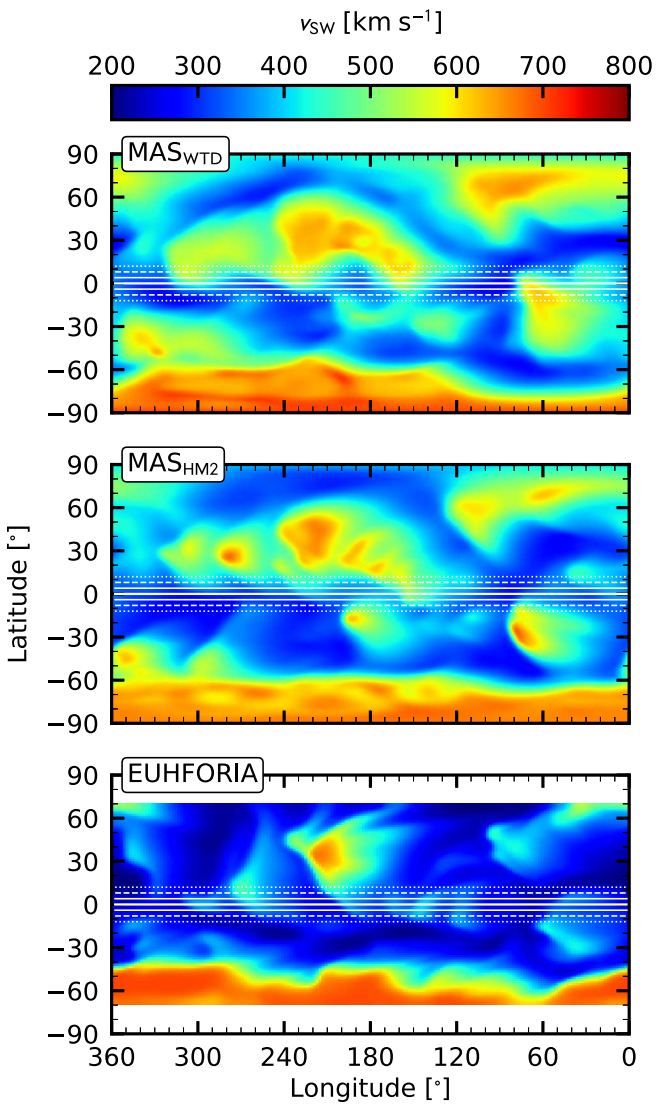

Figure 4. Solar wind solutions of the MHD models (from top to bottom: MAS$_{WTD}$, MAS$_{HM2}$, and EUHFORIA) for 215 $R_\odot$ and the processed ground truth map (MAS) and the ground truth map for EUHFORIA. The white solid, dashed, and dotted lines correspond to $\lambda = 0^\circ$, $\pm 4^\circ$, $\pm 8^\circ$, and $\pm 12^\circ$, respectively. Note that the maps are displayed in counterclockwise longitude to match in situ solar wind profiles.

from Helioseismic and Magnetic Imager (HMI; J. Schou et al. 2012) data. Specifically, we replace the magnetic field above 68.°5 latitude uniformly with the mean value (Figure 2(h)).

Uncertainty due to the resolution and sensitivity of the instrument. Instrument-related uncertainties are highly specific and, therefore, difficult to assess accurately. Instead, we chose to simulate common preprocessing adjustments applied to magnetic maps for modeling purposes, specifically changes in resolution and smoothing. To do this, we doubled, halved, and quartered the pixel resolution of the synoptic charts while ensuring flux conservation (Figures 2(d)–(f)). We also applied various Gaussian filters uniformly across the entire synoptic chart, using six kernels with sizes of 0.°5, 1.°0, 1.°5, 2.°0, 2.°5, and 3.°0 to remove different scales of information (Figures 3(k)–(p)).

In total, this leads to 16 different maps (including the ground truth map) that we used as input to different solar wind models.

3. Methods

To obtain a measure of the uncertainties, we run the created set of input magnetograms with three different solar wind prediction models and analyze their variations. In addition, we use the preprocessed ground truth map with the thermodynamic Magnetohydrodynamic Algorithm outside a Sphere (MAS; Z. Mikić & J. A. Linker 1996; Z. Mikić et al. 1999) model using two different configurations for the heating function in the coronal model part. The MAS code solves time-dependent resistive thermodynamic MHD equations in three-dimensional spherical coordinates to derive the plasma and magnetic field of the corona and the ambient solar wind taking into account a realistic energy equation with anisotropic thermal conduction, radiative losses, and coronal heating. The two different heating configurations are referred to as MAS$_{HM2}$ and MAS$_{WTD}$, respectively, and described in Appendix A.2.

We run all 16 maps (i.e., the ground truth map input map plus its 15 different variations) using the Wang–Sheeley–Arge (WSA) model (C. N. Arge & V. J. Pizzo 2000), an operational solar wind forecasting tool that combines a potential field source surface (PFSS) model (M. D. Altschuler & G. Newkirk 1969) with a Schatten current sheet (SCS; K. H. Schatten 1971) model to construct the coronal magnetic field. The results are then fed into an empirical solar wind relation to estimate the solar wind at the inner boundary and subsequently propagated to Earth using the one-dimensional kinematic solar wind model within WSA, which simulates the quasi-ballistic propagation of hypothetical solar wind macro-particles through the heliosphere. The same maps are also run with the Heliospheric Upwind eXtrapolation model with time dependence (HUXt; M. J. Owens et al. 2020; L. Barnard & M. Owens 2022). HUXt is a computationally efficient, open-source solar wind model with reduced physics that we coupled to the coronal output of the WSA model at 21.5 $R_\odot$. And lastly we use the European Heliospheric FORecasting Information Asset (EUHFORIA; J. Pomoell & S. Poedts 2018). It is a three-dimensional MHD model of the inner heliosphere, typically extending to several au that is coupled with a coronal model consisting of a PFSS model and an SCS model extending to the inner boundary of 21.5 $R_\odot$. For more details on these models, see Appendix A.

4. Results

4.1. MHD View of the Heliosphere

We can compare the coronal and heliospheric structures using the MAS model results. Our analysis assumes that the ground truth map accurately represents the concurrent state of the solar magnetic field at any given time. By combining this map with the MAS model, which incorporates comprehensive physics, we gain valuable insights. However, due to uncertainties in the setup and initial conditions of MHD models (e.g., heating function and plasma parameters), the MAS runs may not necessarily produce a heliosphere that is closer to the ground truth than other models. Therefore, we compare the operational model results with the MAS runs to assess the spread of model solutions, and not as a metric of model accuracy. Figure 4 shows the solar wind structure near Earth's orbit at 215 $R_\odot$ for the MAS runs as well at the EUHFORIA run with the ground truth map. The most notable feature is a prominent high-speed stream (HSS) extending over at least 100° in longitude. However, the equatorial cut (indicated by

the central white line) does not continuously traverse this region; instead, it intersects the high-speed portion multiple times. Both MAS model runs exhibit slight structural differences in the latitude range near Earth's assumed location (presumed as $\lambda = 0°$), leading to variations in the measured solar wind profile. Sensitivity in the solar wind speed due to slight variations of the target latitude can be seen by using additional latitudinal cuts (at $\lambda = \pm 4°$, $\pm 8°$, and $\pm 12°$). For our MAS runs, this results in local changes ($|\Delta v|$) of the solar wind speed of up to 125, 188, and 283 km s^{-1} for $\lambda = \pm 4°$, $\pm 8°$, and $\pm 12°$, respectively (see Figure 7). The solar wind profiles are correlated with a Pearson correlation coefficient of $cc_{\mathrm{Pearson}} = 0.41$ and a value for the Hanna and Heinold metric of $\mathrm{HH}_{||} = 0.23$ (Equation (11) in Table 2) and the root mean square error (RMSE; Equations (4) and 10 in Table 2) between the two profiles is 87.1 ± 65.3 km s^{-1}. This demonstrates that even small changes in the MHD model can significantly impact the measured speed, emphasizing that minor uncertainties in model parameters can result in substantial uncertainties in the outcomes. In the EUHFORIA model, the HSS is significantly smaller in longitudinal and latitudinal extent and is only intersected by $\lambda \geqslant 4°$.

4.2. Uncertainties within the Different Models

We investigate the uncertainties within each model caused by the different modified input maps to determine the uncertainty range. All 16 maps are used as input to HUXt, WSA, and EUHFORIA to predict the solar wind speed at Earth's assumed location ($\lambda = 0°$), as shown in Figure 5. The results generally show a similar structure across all models: a short HSS followed by an extended HSS (approximately 100° longitude), and then another shorter one. However, significant differences emerge as not all these parts are captured by all models and maps. The trailing stream specifically is not captured by all runs, although those using the ground truth map notably all capture it. Furthermore, we observe that the full range of results using the modified maps does not always encompass the outcomes from the ground truth map runs, i.e., the true solution might not lie within the range of uncertain (modified) maps. Whereas for the HUXt runs the ensemble median corresponds quite well to the ground truth map run (RMSE is 58.6 km s^{-1}, $cc_{\mathrm{Pearson}} = 0.75$, and $\mathrm{HH}_{||} = 0.12$), for WSA there is a notable difference (RMSE is 86.9 km s^{-1}, $cc_{\mathrm{Pearson}} = 0.51$, and $\mathrm{HH}_{||} = 0.19$), and EUHFORIA even appears to be anticorrelated (RMSE is 120.9 km s^{-1}, $cc_{\mathrm{Pearson}} = -0.49$, and $\mathrm{HH}_{||} = 0.38$). For more detailed statistics see Table 3 in Appendix B.

But as shown in the MAS model results, small latitudinal differences can significantly impact the predicted solar wind velocity. To investigate the additional uncertainties arising from this effect, we computed the solar wind speed for all models and maps at additional latitudinal positions ($\lambda = \pm 4°$, $\pm 8°$, and $\pm 12°$). We then determined the deviation of the runs using the ground truth map from the corresponding solar wind velocities derived from these latitude intervals, i.e., a larger latitude interval leads to a broader predicted range of solar wind velocities and is, therefore, more likely to encompass the ground truth map run.

Figure 6 presents this deviation as the root mean square deviation (RMSD; see Equation (12) in Table 2) as a function of the latitude interval. We find that extending the latitude interval to $\lambda = \pm 4°$, $\pm 8°$, and $\pm 12°$ results in average velocity intervals ($\Delta\bar{v}$) of 48, 76, and 106 km s^{-1}, respectively. Note

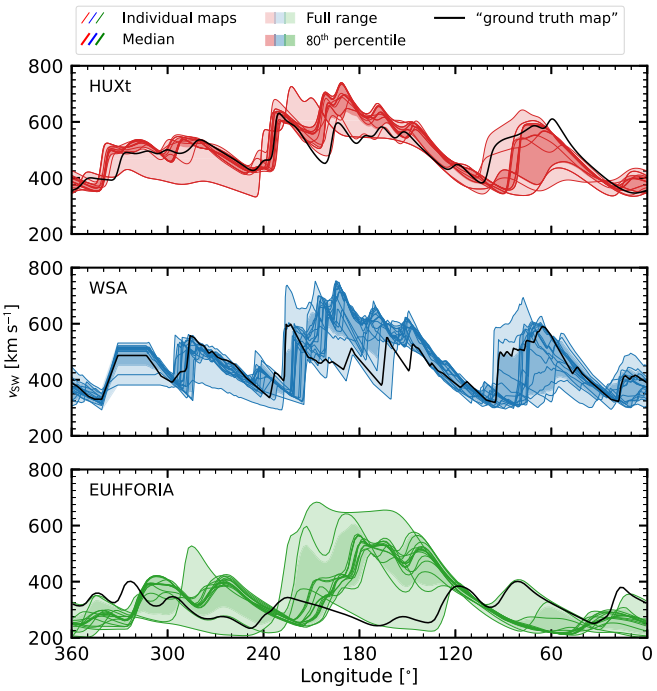

Figure 5. Forecast solar wind speeds for HUXt, WSA, and EUHFORIA (top to bottom). The black line represents the run with the ground truth map, the thin lines are all the runs using the modified maps, the thick line is the median of all the runs, and the shaded areas are the 80th and 100th percentiles. The x-axis represents counterclockwise longitude corresponding to the in situ solar wind of a rotated steady-state solution at a stationary measurement point.

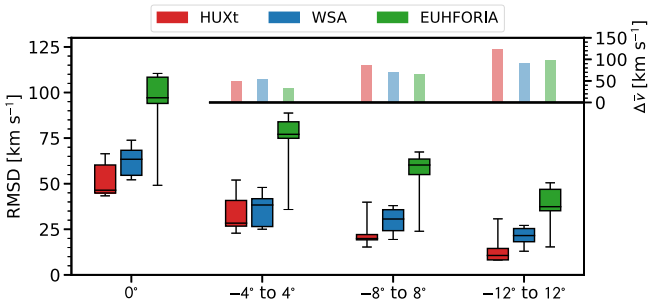

Figure 6. Deviation (RMSD) of the runs using the ground truth map compared to modified runs at $\lambda = 0°$ and in the $\pm 4°$, $\pm 8°$, and $\pm 12°$ intervals. The central bar corresponds to the median of all 15 modified map results, the box represents the 20th and 80th percentiles, and the error bars correspond to the 10th and 90th percentiles. The average size of the respective velocity intervals ($\Delta\bar{v}$) is shown in the top right.

that each latitude interval encompasses all solutions within its range. For instance, the $\pm 4°$ interval includes the solutions at $+4°$, $-4°$, and $0°$. By doing so, the RMSD (for one profile, e.g., at $\lambda = 0°$ the RMSD defaults to the RMSE) decreases by 20%–40%, 38%–57%, and 61%–77% for the different latitude intervals. This demonstrates that expanding the latitude range around the proposed Earth's position can significantly improve the accuracy of forecasts by increasing the likelihood that the ground truth lies within the predicted interval.

For the individual maps, we find little difference in the uncertainties, except for the significant increase in uncertainty when comparing maps based on the ground truth map to those based on the synoptic chart approximation. The RMSE increases by at least 10, 40, and 70 km s^{-1} for HUXt, WSA, and EUHFORIA, respectively.

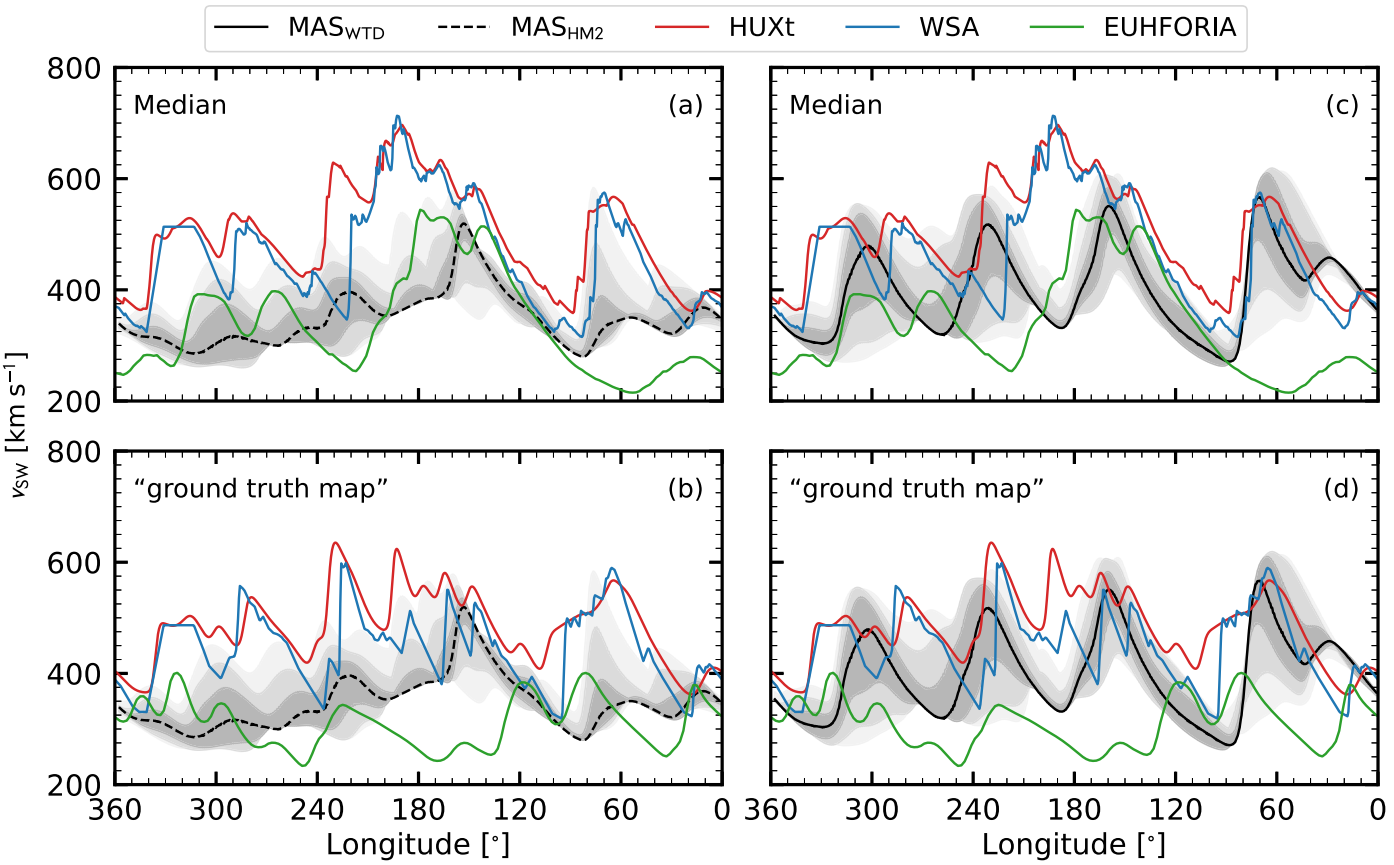

Figure 7. Comparison of the MAS results with the results of the full sample of runs using the modified and ground truth maps. Panels (a) and (b) show the MAS$_{WTD}$ results, while panels (c) and (d) show the MAS$_{HM2}$ results. The solid and dashed lines represent the cut at $\lambda = 0°$ through the steady-state solution, and the shaded areas represent the solar wind in $\lambda = \pm 4°$, $\pm 8°$, and $\pm 12°$ intervals, respectively.

4.3. Uncertainties in Comparison to MAS Model Runs

To better understand the uncertainty ranges when incorporating different models, we compare the solar wind predictions from HUXt, WSA, and EUHFORIA using both the sample median and the results from the ground truth map with the solar wind predictions from the MAS model runs. This comparison is shown in Figure 7. We find that the predictions from the three operational models differ significantly from those of the MAS runs, both in terms of the median of the modified runs and the ground truth map results. While we find that the HUXt and WSA results for the respective sample median and ground truth map run are in good agreement ($HH_{||} = 0.13$ and 0.14 and $cc_{Pearson} = 0.73$ and 0.87), the EUHFORIA runs deviate from both ($0.41 \leqslant HH_{||} \leqslant 0.51$). However, most of these runs are significantly different from the MAS runs. This discrepancy is reflected in the spread of values of HH||, ranging from 0.06 to 0.41, with no clear correlation in most cases. The average RMSE against MAS$_{WTD}$ solar wind solutions is approximately 121 km s^{-1}, ranging from 95 to 135 km s^{-1}. In contrast, RMSE values for the three models compared to MAS$_{HM2}$ results vary more widely, from 77 to 172 km s^{-1}, with a mean of 127 km s^{-1}. And even when considering different latitudinal ranges in the MAS model (gray shaded areas in Figure 7), the agreement does not significantly improve. Further statistics are listed in Table 3 in Appendix B.

5. Discussion and Conclusion

From a solar rotation of synthetic magnetograms, we created a set of modified maps designed to mimic uncertainties in the magnetic field maps caused by incomplete observational constraints. Using this set of input maps, we ran multiple operational solar wind forecasting models to derive a plausible range of values for the forecast and, subsequently, estimated the uncertainties.

Constraining the uncertainties in solar wind predictions has become more important in recent times. L. Bertello et al. (2014) concluded that the uncertainties that arise from creating synoptic charts have a significant impact on the location and structure of the neutral lines and the distribution of the coronal holes, which is paramount for predicting the solar wind at a single point in space, i.e., Earth. This effect can be seen in the runs using the ground truth map and MAS runs where the large central high-speed stream is not traversed continuously. B. Poduval et al. (2020) estimated an uncertainty with an RMSE of 85–110 km s^{-1} in solar wind predictions due to the uncertainties in the photospheric flux density synoptic maps. This is similar to the results derived in this study of 59–121 km s^{-1} for within the individual models and about 77–172 km s^{-1} in comparison to the thermodynamic MAS models using the ground truth map. Further, we show that using a cloud of points in latitude around the target latitude can significantly reduce the uncertainties.

In recent studies, the uncertainties in solar wind forecasting compared to observations for operational models were found to have an RMSE of 100–120 km s^{-1} (see, e.g., M. A. Reiss et al. 2016, 2020; D. Milošić et al. 2023). This value is similar to the results obtained within a single model in comparison to when using the ground truth map maps as input. However, it is important to note that our analysis only compared model runs with an assumed ground truth map and its modifications. We did not account for the fact that none of these models can fully describe the coronal and heliospheric processes.

In summary, we can conclude the following:

1. For each operational model, we find significant variations between the ground truth map run and the modified map runs. The RMSE values within HUXt, WSA, and EUHFORIA are 59, 87, and 121 km s^{-1}, respectively.
2. We find that the largest source of uncertainty stems from the generation of synoptic charts, with the assumption that this is due to the combined impact of the aging effect and the absence of far-side information.
3. For all three models, the ground truth map run does not always fall within the range of modified runs, underscoring that ensemble predictions may not fully capture real solar wind variability. However, considering multiple latitudes rather than a single point reduces forecast uncertainty and lowers the chance of excluding the ground truth map run by 20%–77%.
4. While the HUXt and WSA results are rather similar, the average spread of all the model results is $\Delta\bar{v} = 251$ km s^{-1}.
5. On average, the variations resulting from modifications to the magnetic field input maps, used as a proxy for observational uncertainties, are generally consistent with those found in other studies. Furthermore, the uncertainties within a single model are smaller than the differences between all the models.

While it is possible to quantify the uncertainties arising from incomplete magnetic field information by using a ground truth map as a reference, the true solar wind remains elusive. The processes from solar wind acceleration to its propagation in the heliosphere are not yet fully understood (N. M. Viall & J. E. Borovsky 2020). Our results suggest that increasing the operational coverage of concurrent solar magnetic field observations could reduce the uncertainty in the background solar wind by approximately 100 km s^{-1} near 1 au. Alternatively, predicting a range of velocities arising from a cloud of points around Earth can help mitigate some uncertainties arising from incomplete magnetic field information.

Acknowledgments

We thank the International Space Science Institute (ISSI, Bern) for the generous support of the ISSI teams "Magnetic Open Flux and Solar Wind Structuring in Heliospheric Space" (2019–2021) and "Quantitative Comparisons of Solar Surface Flux Transport Models" (2024–2025). This research was funded in whole, or in part, by the Austrian Science Fund (FWF) Erwin-Schrödinger fellowship J-4560. The open access was funded by Helsinki University Library. S.G.H. thanks Andreas Wagner for valuable discussions. J.P. and S.G.H. acknowledge funding from the Academy of Finland project SWATCH (343581). Work at Predictive Science Inc. was supported by the NASA LWS Strategic Capabilities Program (grant No. 80NSSC22K0893). M.O. was part-funded by Science and Technology Facilities Council (STFC) grant No. ST/V000497/1 and Natural Environment Research Council (NERC) grant NE/Y001052/1. L.A.U. and B.K.J. were supported by the NASA LWS Strategic Capabilities Program (grant No. 80NSSC22K0893) and by NASA grant No. NNH18ZDA001N-DRIVE to the COFFIES DRIVE Center, managed by Stanford University.

Appendix A
Model Setup

In this appendix, we provide additional details about each of the models that were used for the analysis described in the paper (e.g., AFT, MAS, WSA, and HUXt).

A.1. Advective Flux Transport Model

The AFT model solves the horizontal components of the induction equation, similar to other surface flux transport (SFT) models. However, unlike traditional SFT models, AFT employs convective simulations of horizontal surface flows instead of the diffusivity parameter typically used in other models. These convective simulations include both axisymmetric flows (differential rotation and meridional flow) and convective flows (D. H. Hathaway et al. 2010). By incorporating convective simulations, AFT eliminates the need for an explicit diffusion term. However, diffusion is still solved within the model solely to stabilize the numerical scheme (L. Upton & D. H. Hathaway 2014a, 2014b).

To create synthetic full-Sun magnetic data, AFT utilizes the Synthetic Active Region Generator (SARG; B. K. Jha & L. A. Upton 2024), which is incorporated as the source term along with random flux. SARG uses ISSNv2.0 to define the monthly sunspot number (or cycle amplitude) as a function of time. This determines the frequency of active region emergence (for details, see B. K. Jha & L. A. Upton 2024). SARG uses the known statistical properties of solar active regions, such as the location, flux, and polarity (Joy's law and Hale's polarity law), to define these parameters for the synthetic active region. The output is a synthetic active region catalog consisting of latitude, longitude, and flux for each bipole of the active regions. Once all these properties are determined, we generate idealized bipolar Gaussian spots. These spots are added into the model, thus simulating the emergence of magnetic active regions. We note that each active region generated by SARG is added to the model only once at the time of its emergence in SARG.

In this particular study AFT also employs the Gaussian random flux generator (GRaFg), with a mean of zero and a standard deviation of one, to emulate the random emergence of small-scale flux. The random flux values drawn from Gaussian distribution are inserted at random locations, where latitude values are sampled from a cosine distribution and longitude values from a uniform distribution. The GRaFg makes sure that the net flux added into the model is always zero to avoid accumulation of any monopole. The number of random grid points and the frequency of emergence of these random fluxes are optimized to ensure that the total absolute flux in the model remains consistent with the case where no random flux is present. We note that in AFT, these random fluxes have no impact on the global properties of the system. Here, we used

the GRaFg model with a mean of zero and a standard deviation of one, adding random flux values at 1000 grid points every hour.

A.2. Magnetohydrodynamic Algorithm Outside a Sphere Model

The MAS code is an in-production MHD model with over 25 yr of ongoing development used extensively in solar physics research (Z. Mikić et al. 1999, 2018; J. A. Linker et al. 2003, 2011; R. Lionello et al. 2006, 2009a, 2013; C. Downs et al. 2013; T. Török et al. 2018).[6] The code is included in the CORona-HELiosphere (CORHEL) software suite (P. Riley et al. 2012) hosted at NASA's Community Coordinated Modeling Center (CCMC),[7] allowing users to generate quasi-steady-state MHD solutions of the corona and heliosphere, as well as the CORHEL-CME suite (J. A. Linker et al. 2024), which allows users to run MHD simulations of coronal mass ejection (CME) events from the Sun to Earth (J. A. Linker et al. 2024).[8] MAS is written in modern Fortran and parallelized to run across multiple multi-CPU and multi-GPU systems (R. M. Caplan et al. 2023). The MAS code employs a logically rectangular, nonuniform staggered spherical grid and applies finite-difference discretization techniques, utilizing a combination of explicit and implicit time-stepping schemes.

MAS contains numerous coronal heating models, both empirical and physics-based, that can be combined together. Empirical heating can be set by a combination of analytic functions (R. Lionello et al. 2009a). A form of this model that is used in CORHEL is denoted in this work as HM2 (Z. Mikic et al. 2010). The primary physics-based heating approach in MAS is the wave-turbulence-driven (WTD) model (R. Lionello et al. 2014; C. Downs et al. 2016; Z. Mikić et al. 2018) and is denoted as WTD in this work.

A.3. Wang–Sheeley–Arge Model

The WSA model consists of three components. The first, a PFSS model, maps the inner coronal magnetic field from the photosphere to source surface radius (R_{SS}) using a spherical harmonic expansion to match photospheric flux and enforce radial field at the source surface. The second component extends the field solution from the SCS radius (R_{SCS}) to 5 $R_\odot$ using the SCS model. This approach creates a current sheet and helmet streamer above the neutral line by temporarily enforcing positive radial field values and solving a potential field problem, ensuring open field lines remain open and minimizing energy. The final component uses the field at 5 $R_\odot$ to derive the wind speed, based on an empirical formula that considers the local magnetic flux expansion, f_{exp}, and the distance to the nearest coronal hole boundary, Θ_B.

For the WSA performed in this study, we used $R_{SS} = 2.51\ R_\odot$, $R_{ScS} = 2.49\ R_\odot$ as well as the empirical solar wind relation:

$$V = V_0 + \frac{V_m}{(1+f_{exp})^{C_1}}\left(1 - C_2 \exp\left[-\left(\frac{\Theta_B}{C_3}\right)^{C_4}\right]\right)^{C_5}, \quad \text{(A1)}$$

Table 1
Parameter Values Used for Solar Wind Speed Predictions in Equation (A1)

V_0 (m s^{-1})	V_m (m s^{-1})	C_1	C_2	C_3	C_4	C_5
286	625	2/9	0.8	1	2	3

where V_0, V_m, and C_1–C_5 are empirically determined parameters given in Table 1.

A.4. Heliospheric Upwind EXtrapolation with Time Dependence Model

HUXt (M. J. Owens et al. 2020; L. Barnard & M. Owens 2022) is a numerical model that approximates the solar wind as a one-dimensional, incompressible hydrodynamic flow (see also P. Riley & R. Lionello 2011). Consequently, solar wind flows are dynamic and may accelerate and decelerate through stream interaction, but only solar wind speed (and not other plasma parameters) is reconstructed. Despite the approximations employed, HUXt produces solar wind speed structure throughout the model domain (typically from 0.1 to 1.5 au) that agrees very closely with the results of three-dimensional MHD models for the same boundary conditions (M. J. Owens et al. 2020), but at a fraction of the computational cost. This allows for large parametric studies, and for ensemble forecasting and data assimilation techniques to be more easily employed.

A.5. EUropean Heliospheric FOrecasting Information Asset

EUHFORIA is a framework for modeling global-scale dynamics in the inner heliosphere. Given information of the plasma and magnetic field at the heliospheric inner boundary set at a heliocentric radius of $r_H = 0.1$ au, the evolution of the solar wind for $r > r_H$ is determined by solving the MHD equations in three dimensions, as detailed in J. Pomoell & S. Poedts (2018).

The ambient state of the solar wind at $r = r_H$ can be prescribed in various ways. Commonly and for the runs used in this work, it is constructed using a semi-empirical prescription akin to the approach employed by the WSA model (see A.3). First, the magnetic field in the coronal domain ($r \in [R_\odot, r_H]$) is modeled using the PFSS model in the lower corona and a current sheet model in the upper corona. In this work, these models are computed using a finite-difference approach, and with the source surface radius in the PFSS model set to 2.51 $R_\odot$ and the inner radial boundary of the current sheet model set at 2.49 $R_\odot$. The choice of these parameters can have a significant influence on the resulting magnetic field structure (e.g., E. Asvestari et al. 2019), and were here chosen to be the same as those used by the WSA model. Before computation, the (numerical) signed flux in the considered magnetic maps was balanced to zero using a multiplicative method. The computation employed a constant radial grid spacing of $\Delta r \sim 0.005\ R_\odot$ in the PFSS model and $\Delta r \sim 0.05\ R_\odot$ in the current sheet mode, and a 1° angular grid spacing as given by the magnetic maps.

Using the coronal model, the connectivity of the magnetic field is determined by tracing field lines, and a map of the (great circle) distance d to nearest open field regions constructed. The wind speed is then determined using the

[6] https://www.predsci.com/mas
[7] https://ccmc.gsfc.nasa.gov
[8] https://ccmc.gsfc.nasa.gov/models/CORHEL-CME~1

empirical prescription given by

$$V = V_s + \frac{1}{2}(V_f - V_s)\left(1 + \tanh\left(\frac{d - d_0}{w}\right)\right), \quad \text{(A2)}$$

where $V_f = 720\,\mathrm{km\,s^{-1}}$, $V_s = 220\,\mathrm{km\,s^{-1}}$, $d_0 = 2°$, and $w = 2°$. A similar empirical relation was studied in P. Riley et al. (2015). Based on the obtained empirical solar wind speed, the boundary data for the MHD computation are determined as described in J. Pomoell & S. Poedts (2018), with the following modifications. First, the the absolute value of the radial magnetic field at r_H is constant and chosen to provide an equal unsigned flux as the unsigned open flux given by the coronal model while the field polarity is given directly by the coronal model, and second, the wind speed is reduced not by a constant but instead by using $v_r = V - (40\,\mathrm{km/s})\frac{600\,\mathrm{km\,s^{-1}}}{V}$.

The heliospheric MHD computation is run for a duration of 10 days until an approximate steady-state solar wind solution is reached (no CMEs were launched). The simulation domain encompassed a radial domain $r \in [0.1, 1.5]$ au and a latitudinal domain $\lambda \in [-70°, 70°]$. A uniform grid using (300, 93, 180) cells in the radial, latitudinal, and longitudinal directions was employed.

Appendix B
Statistics

Table 2 lists the metrics used in this study and Table 3 shows the statistics of the runs using the modified maps to those using the ground truth map.

Table 2
Summary of Statistical Metrics Used

No.	Name	Abbrev.	Equation
1	Mean absolute deviation	MAD	$\mathrm{MAD} = \frac{1}{n}\sum_{i=1}^{n}\lvert M_i - T_i\rvert$
2	Mean error	ME	$\mathrm{ME} = \frac{1}{n}\sum_{i=1}^{n}(M_i - T_i)$
3	Mean squared error	MSE	$\mathrm{MSE} = \frac{1}{n}\sum_{i=1}^{n}(M_i - T_i)^2$
4	Root mean squared error	RMSE	$\mathrm{RMSE} = \sqrt{\mathrm{MSE}}$
5	Mean percentage error	MPE	$\mathrm{MPE} = \frac{1}{n}\sum_{i=1}^{n}\frac{M_i - T_i}{T_i} \times 100$
6	Std dev. of MAD	σ_{MAD}	$\sigma_{\mathrm{MAD}} = \sqrt{\frac{1}{n-1}\sum_{i=1}^{n}(\lvert M_i - T_i\rvert - \mathrm{MAD})^2}$
7	Std dev. of ME	σ_{ME}	$\sigma_{\mathrm{ME}} = \sqrt{\frac{1}{n-1}\sum_{i=1}^{n}((M_i - T_i) - \mathrm{ME})^2}$
8	Std dev. of MSE	σ_{MSE}	$\sigma_{\mathrm{MSE}} = \sqrt{\frac{1}{n-1}\sum_{i=1}^{n}((M_i - T_i)^2 - \mathrm{MSE})^2}$
9	Std dev. of MPE	σ_{MPE}	$\sigma_{\mathrm{MPE}} = \sqrt{\frac{1}{n-1}\sum_{i=1}^{n}\left(\frac{M_i - T_i}{T_i} \times 100 - \mathrm{MPE}\right)^2}$
10[a]	Std dev. of RMSE	σ_{RMSE}	$\sigma_{\mathrm{RMSE}} \approx \frac{1}{2\sqrt{\mathrm{MSE}}} \cdot \sigma_{\mathrm{MSE}}$
11[b]	Hanna and Heinold metric	$\mathrm{HH}_{\lVert}$	$\mathrm{HH}_{\lVert} = \sqrt{\frac{\sum_{i=1}^{n}\lvert M_i - T_i\rvert^2}{\sum_{i=1}^{n}\lvert M_i\rvert\lvert T_i\rvert}}$
12[c]	Root mean square deviation	RMSD	$\mathrm{RMSD} = \begin{cases} 0, & \text{if } L_i \leqslant T_i \leqslant U_i \\ \sqrt{\frac{1}{n}\sum_{i=1}^{n}(L_i - T_i)^2}, & \text{if } T_i < L_i \\ \sqrt{\frac{1}{n}\sum_{i=1}^{n}(U_i - T_i)^2}, & \text{if } T_i > U_i \end{cases}$

Notes. M_i: value of runs using modified maps (or median value). L_i: lower bound. U_i: upper bound. T_i: value of run using the ground truth model. n: total number of data points.

[a] Approximated using delta method.

[b] We are calculating an absolute value version of the Hanna and Heinold metric (S. R. Hanna & D. W. Heinold 1986) because it provides a normalized, scale-invariant measure of similarity between two time series. By accounting for both the differences and the magnitudes of the data points, this metric allows us to compare the relative shapes and patterns of the series regardless of their absolute scale. This error metric has been demonstrated to be more effective for evaluating numerical solutions compared to the more commonly used normalized root mean square (RMSE) error metric (L. Mentaschi et al. 2013).

[c] Given two data series representing the lower and upper bounds, RMSD quantifies the deviation of a comparison data series from this interval. If the lower and upper bounds are identical RMSD defaults to RMSE.

Table 3
Statistics of the Deviation of the Median of the Runs Using the Modified Maps and Those Using the Ground Truth Map against the Two Runs Using the MAS Model (MAS_{HM2} and MAS_{WTD})

Model	MAD (km s^{-1})	σ_{MAD} (km s^{-1})	ME (km s^{-1})	σ_{ME} (km s^{-1})	RMSE (km s^{-1})	σ_{RMSE} (km s^{-1})	MPE (%)	σ_{MPE} (%)	D_{max} (km s^{-1})	$HH_{\|\|}$	$cc_{Pearson}$
Median of Modified Runs versus Ground Truth Map Runs											
HUXt	41.8	42.0	10.7	58.3	59.2	58.6	2.4	11.7	203.1	0.12	0.75
WSA	56.5	66.1	17.2	85.3	86.9	84.8	4.4	18.3	268.6	0.19	0.51
EUHFORIA	94.8	75.2	25.1	118.5	120.9	88.6	12.4	42.4	287.3	0.38	−0.49
Median of Modified Runs versus MAS_{HM2}											
WSA	114.1	90.6	112.8	92.3	145.7	90.5	33.6	27.8	359.9	0.36	0.35
HUXt	151.8	80.5	151.8	80.5	171.8	75.6	44.8	24.4	332.8	0.41	0.42
EUHFORIA	64.4	42.3	−10.2	76.5	77.1	40.8	−2.8	21.9	163.8	0.22	0.53
Runs with the Ground Truth Map versus MAS_{HM2}											
WSA	98.7	76.8	96.3	79.8	125.0	73.7	29.9	25.9	269.5	0.32	0.06
HUXt	142.3	74.5	141.3	76.5	160.6	66.2	42.7	25.1	272.9	0.39	0.21
EUHFORIA	63.3	55.2	−36.1	75.8	83.9	72.1	−8.3	19.9	244.6	0.26	−0.33
Median of Modified Runs versus MAS_{WTD}											
WSA	91.8	82.3	61.2	107.0	123.2	101.6	18.2	29.2	354.6	0.29	0.24
HUXt	109.8	78.8	100.2	90.7	135.1	96.4	27.9	26.2	363.4	0.30	0.39
EUHFORIA	101.6	80.3	−61.8	113.8	129.4	92.0	−12.8	25.6	333.6	0.35	0.06
Runs with the Ground Truth Map versus MAS_{WTD}											
WSA	72.1	61.5	44.7	83.6	94.7	69.6	14.4	25.2	246.6	0.22	0.30
HUXt	99.3	63.5	89.7	76.5	117.9	71.1	25.5	24.4	272.0	0.27	0.44
EUHFORIA	109.7	67.0	−87.7	94.0	128.5	69.8	−18.7	21.9	292.7	0.37	−0.20

Note. From left to right: mean absolute error (MAD) and the standard deviation of MAD (σ_{MAD}), the mean square error (MSE) and the standard deviation of the MSE (σ_{MSE}), the root mean square error (RMSE) and the error in the RMSE (σ_{RMSE}), the maximum deviation (D_{max}), and the absolute Hanna and Heinold metric ($HH_{||}$).

ORCID iDs

Stephan G. Heinemann https://orcid.org/0000-0002-2655-2108
Jens Pomoell https://orcid.org/0000-0003-1175-7124
Ronald M. Caplan https://orcid.org/0000-0002-2633-4290
Mathew J. Owens https://orcid.org/0000-0003-2061-2453
Shaela Jones https://orcid.org/0000-0001-9498-460X
Lisa Upton https://orcid.org/0000-0003-0621-4803
Bibhuti Kumar Jha https://orcid.org/0000-0003-3191-4625
Charles N. Arge https://orcid.org/0000-0001-9326-3448

References

Altschuler, M. D., & Newkirk, G. 1969, SoPh, 9, 131
Arge, C. N., Henney, C. J., Koller, J., et al. 2010, in AIP Conf. Proc. 1216, Twelfth International Solar Wind Conference, ed. M. Maksimovic (Melville, NY: AIP), 343
Arge, C. N., & Pizzo, V. J. 2000, JGR, 105, 10465
Asvestari, E., Heinemann, S. G., Temmer, M., et al. 2019, JGRA, 124, 8280
Barnard, L., & Owens, M. 2022, FrP, 10, 1005621
Bertello, L., Pevtsov, A. A., Petrie, G. J. D., & Keys, D. 2014, SoPh, 289, 2419
Caplan, R. M., Stulajter, M. M., & Linker, J. A. 2023, in 2023 IEEE Int. Parallel and Distributed Processing Symp. Workshops (IPDPSW) (IEEE) (Piscataway, NJ: IEEE), 582
Caplan, R. M., Stulajter, M. M., Linker, J. A., et al. 2025, ApJS, 278, 24
Case, A. W., Spence, H. E., Owens, M. J., Riley, P., & Odstrcil, D. 2008, GeoRL, 35, L15105
Downs, C., Linker, J. A., Caplan, R. M., et al. 2025, Sci, in press
Downs, C., Linker, J. A., Mikić, Z., et al. 2013, Sci, 340, 1196
Downs, C., Lionello, R., Mikić, Z., Linker, J. A., & Velli, M. 2016, ApJ, 832, 180
Hanna, S. R., & Heinold, D. W. 1986, Simple Statistical Methods for Comparative Evaluation of Air Quality Models (Boston, MA: Springer), 441
Hathaway, D. H., Williams, P. E., Dela Rosa, K., & Cuntz, M. 2010, ApJ, 725, 1082
Heinemann, S. G., Temmer, M., Hofmeister, S. J., et al. 2021, SoPh, 296, 141
Hinterreiter, J., Magdalenic, J., Temmer, M., et al. 2019, SoPh, 294, 170
Jha, B. K., & Upton, L. A. 2024, ApJL, 962, L15
Jian, L. K., MacNeice, P. J., Taktakishvili, A., et al. 2015, SpWea, 13, 316
Linker, J. A., Lionello, R., Mikić, Z., Titov, V. S., & Antiochos, S. K. 2011, ApJ, 731, 110
Linker, J. A., Mikić, Z., Lionello, R., et al. 2003, PhPl, 10, 1971
Linker, J. A., Torok, T., Downs, C., et al. 2024, JPhCS, 2742, 012012
Lionello, R., Downs, C., Linker, J. A., et al. 2013, ApJ, 777, 76
Lionello, R., Linker, J. A., & Mikić, Z. 2009a, ApJ, 690, 902
Lionello, R., Linker, J. A., Mikić, Z., & Riley, P. 2006, ApJL, 642, L69

Lionello, R., Velli, M., Downs, C., et al. 2014, ApJ, 784, 120
Mentaschi, L., Besio, G., Cassola, F., & Mazzino, A. 2013, OcMod, 72, 53
Mikić, Z., Downs, C., Linker, J. A., et al. 2018, NatAs, 2, 913
Mikić, Z., & Linker, J. A. 1996, in AIP Conf. Ser. 382, Proc. of the Eighth Int. Solar Wind Conf.: Solar Wind Eight, ed. D. Winterhalter et al. (Melville, NY: AIP), 104
Mikic, Z., Linker, J. A., Lionello, R., Riley, P., & Titov, V. S. 2010, AGUFM, 2010, SH42A
Mikić, Z., Linker, J. A., Schnack, D. D., Lionello, R., & Tarditi, A. 1999, PhPl, 6, 2217
Milošić, D., Temmer, M., Heinemann, S. G., et al. 2023, SoPh, 298, 45
Müller, D., St. Cyr, O. C., Zouganelis, I., et al. 2020, A&A, 642, A1
Odstrčil, D., & Pizzo, V. J. 1999, JGR, 104, 483
Owens, M. J., Lang, M., Barnard, L., et al. 2020, SoPh, 295, 43
Owens, M. J., Spence, H. E., McGregor, S., et al. 2008, SpWea, 6, S08001
Perri, B., Finley, A., Réville, V., et al. 2024, A&A, 687, A10
Poduval, B., Petrie, G., & Bertello, L. 2020, SoPh, 295, 138
Pomoell, J., Lumme, E., & Kilpua, E. 2019, SoPh, 294, 41
Pomoell, J., & Poedts, S. 2018, JSWSC, 8, A35
Posner, A., Arge, C. N., Staub, J., et al. 2021, SpWea, 19, e2021SW002777
Reiss, M. A., MacNeice, P. J., Muglach, K., et al. 2020, ApJ, 891, 165
Reiss, M. A., Muglach, K., Mullinix, R., et al. 2023, AdSpR, 72, 5275
Reiss, M. A., Temmer, M., Veronig, A. M., et al. 2016, SpWea, 14, 495
Riley, P., Linker, J. A., & Arge, C. N. 2015, SpWea, 13, 154
Riley, P., Linker, J. A., Lionello, R., & Mikic, Z. 2012, JASTP, 83, 1
Riley, P., Linker, J. A., Mikic, Z., et al. 2019, ApJ, 884, 18
Riley, P., & Lionello, R. 2011, SoPh, 270, 575
Rotter, T., Veronig, A. M., Temmer, M., & Vršnak, B. 2012, SoPh, 281, 793
Rotter, T., Veronig, A. M., Temmer, M., & Vršnak, B. 2015, SoPh, 290, 1355
Schatten, K. H. 1971, CosEl, 2, 232
Schou, J., Scherrer, P. H., & Bush, R. I. 2012, SoPh, 275, 229
Solanki, S. K., del Toro Iniesta, J. C., Woch, J., et al. 2020, A&A, 642, A11
Temmer, M., Hinterreiter, J., & Reiss, M. A. 2018, JSWSC, 8, A18
Temmer, M., Scolini, C., Richardson, I. G., et al. 2023, arXiv:2308.04851
Török, T., Downs, C., Linker, J. A., et al. 2018, ApJ, 856, 75
Upton, L., & Hathaway, D. H. 2014a, ApJ, 780, 5
Upton, L., & Hathaway, D. H. 2014b, ApJ, 792, 142
Viall, N. M., & Borovsky, J. E. 2020, JGRA, 125, e26005
Yang, D., Heinemann, S. G., Cameron, R. H., & Gizon, L. 2024, SoPh, 299, 161